

# Journal of Biomedical Optics

[SPIEDigitalLibrary.org/jbo](http://SPIEDigitalLibrary.org/jbo)

## **Wide velocity range Doppler optical microangiography using optimized step-scanning protocol with phase variance mask**

Lei Shi  
Jia Qin  
Roberto Reif  
Ruikang K. Wang

# Wide velocity range Doppler optical microangiography using optimized step-scanning protocol with phase variance mask

Lei Shi, Jia Qin, Roberto Reif, and Ruikang K. Wang

University of Washington, Department of Bioengineering, Seattle, Washington 98195

**Abstract.** We propose a simple and optimized method for acquiring a wide velocity range of blood flow using Doppler optical microangiography. After characterizing the behavior of the scanner in the fast scan axis, a step-scanning protocol is developed by utilizing repeated A-scans at each step. Multiple velocity range images are obtained by the high-pass filtering and Doppler processing of complex signals between A-scans within each step with different time intervals. A phase variance mask is then employed to segment meaningful Doppler flow signals from noisy phase background. The technique is demonstrated by imaging *in vivo* mouse brain with skull left intact to provide bidirectional images of cerebral blood flow with high quality and wide velocity range. © The Authors. Published by SPIE under a Creative Commons Attribution 3.0 Unported License. Distribution or reproduction of this work in whole or in part requires full attribution of the original publication, including its DOI. [DOI: [10.1117/1.JBO.18.10.106015](https://doi.org/10.1117/1.JBO.18.10.106015)]

Keywords: optical coherence tomography; optical microangiography; Doppler velocimetry; step scanning; correlation degree; phase variance.

Paper 130401RR received Jun. 10, 2013; revised manuscript received Oct. 4, 2013; accepted for publication Oct. 9, 2013; published online Oct. 28, 2013.

## 1 Introduction

Doppler optical microangiography (DOMAG)<sup>1</sup> is a technological extension to Doppler optical coherence tomography (DOCT),<sup>2</sup> in which DOCT is combined with recently developed OMAG technique<sup>3</sup> to provide velocity mapping of blood flows within tissue beds *in vivo*. Due to its simple system and algorithm implementation, phase-resolved technique<sup>2</sup> is often used to deduce the axial flow velocity,  $V_z = \lambda\phi/(4\pi nT)$ , where  $\lambda$  is the center wavelength of the light source,  $n$  is the tissue refractive index, and  $\phi$  and  $T$  are the phase difference and time interval between adjacent A-scans, respectively. The maximal and minimal velocities that are detectable in one B-scan [or three-dimensional (3-D) scan] are determined by the time interval  $T$ , the  $\pi$ -ambiguity and the system phase noise level.<sup>2</sup> The shorter  $T$ , i.e., faster imaging speed, is usually required to map the velocities of faster flow, but at an expense of slower ones and vice versa. Therefore, it is currently difficult for DOMAG/DOCT to provide the read-out of blood flows within tissue beds that have wide velocity distributions. However, capability to simultaneously capture blood flow velocities at different ranges from arteries and veins down to capillary vessels is important for comprehensive study of vascular responses in a number of diseases that have vascular components, for example, in the investigation of cerebral blood flow (CBF) responses to a neurological insult, e.g., stroke.<sup>4,5</sup> This is because flow velocity within cerebral cortex exhibits a wide range of values, from tens of micrometer/seconds in capillaries to tens of millimeter/seconds in middle cerebral artery (MCA).

We notice that there are a number of methods previously reported in OCT angiography<sup>6–8</sup> that were tuned to image the

fast or slow flows. Most of these methods employ a linear scan (L-scan) in the fast axis [Fig. 1(a)]. They are, however, not amenable to the requirement of concurrently obtaining the fast and slow velocities provided that just one 3-D scan is performed. By skipping A-scans for DOCT processing, it is possible to obtain multiple velocity ranges within one scan.<sup>6</sup> However, the tissue of interest is often highly scattering and heterogeneous, leading to decreased correlation degree (CD) between A-scans.<sup>9</sup> Note that the high degree of correlation is an utmost requirement for Doppler algorithm to accurately evaluate flow velocity. To increase the degree of correlation, normally the B-scan has to be densely sampled, which, however, translates to reducing the frame rate of the system, not suitable for *in vivo* imaging. The situation is even worse in the case of using skipping A-scan approach to obtain multiple velocity ranges. To mitigate this problem, Meemon and Rolland<sup>10</sup> used a step-scan strategy in the fast axis to obtain multiple velocity ranges, in which the scanner is driven by a stepped waveform while M-mode scan (i.e., repeated A-scan) is employed in each step. The assumption here is that the M-mode scan in each step provides 100% correlation between any two A-scans that are used to deduce the flow velocity. This is true in an ideal situation. However, in practice when the scanner switches from one step to next, it requires some time for the scanner to settle due to its mechanical inertia. Thus, the correlation between any two A-scans in each step is highly dependent upon the mechanical stability of the scanner used. In addition, due to the communication between the computer, the scanner, and the data acquisition device, this settling time is also sometimes system dependent. Consequently, the scanner behavior in the setting of entire system has to be systematically characterized so that an improved step-scan strategy can be devised to optimize the system capability to provide the imaging of wide velocity range. To meet with this requirement, this article proposes an alternative method that is able to provide multirange DOMAG

Address all correspondence to: Ruikang K. Wang, University of Washington, Department of Bioengineering, Seattle, Washington 98195. Tel: 206 6165025; Fax: 206-685-3300; E-mail: [wangrk@uw.edu](mailto:wangrk@uw.edu)

(mDOMAG) with high signal quality based on a common spectral domain OCT (SD-OCT) system setup. Below, we first demonstrate the necessity for characterizing the scanner behavior during scanning for step-scan (S-scan) strategy to provide a multirange velocity map. We then propose an optimized method in which S-scan is employed in the fast axis while a number of repeated A-scans at each step are acquired only after the scanner has been stabilized.

## 2 System Setup and Methods

We employed a fiber-based SD-OCT system to demonstrate the necessity and utility of the proposed optimized step-scan strategy. The SD-OCT system was similar to that previously described.<sup>1</sup> The center wavelength of the light source was  $\lambda = 1310$  nm and both axial and lateral resolutions were  $\sim 10$   $\mu\text{m}$ . The detection unit was a fast spectrometer in which a line InGaAs camera was used to capture the interferograms formed between the lights that were back reflected from the reference and sample arms. The x-y scanner was used in the sample arm to scan a focused beam spot over the sample to acquire volumetric dataset, representing tissue morphology and microcirculations. The system had a measured dynamic range of 105 dB with the light power of 5 mW at sample surface. For experiments reported below, the imaging speed of the system used was 75 kHz A-scan rate.

We first performed experiments to characterize the behavior of the scanner during M-mode scan, upon which to design the optimized scanning pattern. In experiments, we used a stationary cardboard as the sample. In this case, the complication for *in vivo* tissue such as tissue motion or cell swelling/shrink would be absent, facilitating the use of a correlation approach to characterize the OCT signals to achieve our purpose. The fast axis scanner was driven by a step waveform with 400 steps for one B-scan. In each step,  $N = 50$  A-scans were acquired, thus the total number of A-scans in each B-scan was 20,000. In the slow axis direction, we captured 200 B-frames to accomplish one 3-D scan covering an area of  $2 \times 2$  mm<sup>2</sup>. For each B-scan, the absolute values of CD between the  $i$ 'th and  $(i + k)$ 'th A-scans were calculated, where  $k$  is the number of skipped

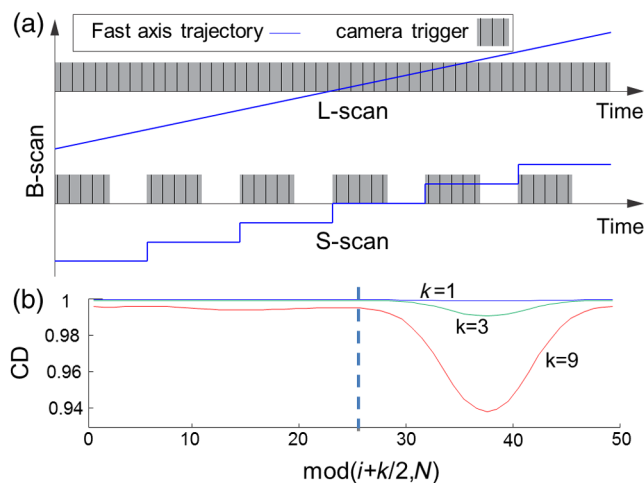


**Fig. 1** Comparison between S- and L-scans in terms of degree of correlation between skipped A-scans. (a) Schematic of L- and S-scan patterns and camera triggers within one B-scan. (b) Absolute values of the degree of correlation averaged according to the remainder of  $(i + k/2)$  divided by  $N$  for S-scan when the system images a stationary cardboard.

A-scans. In this study, we selected  $k = 1, 3,$  and  $9$  to provide three ranges of velocities, corresponding to  $\pm 18.2, \pm 6.1,$  and  $\pm 2$  mm/s, respectively, assuming that the refractive index of tissue is 1.35. Finally, CDs were averaged throughout the 3-D scan according to  $\text{mod}(i + k/2, N)$ , which was the remainder of  $(i + k/2)$  divided by  $N$ . The results are given in Fig. 1(b). We found that for the system used for this study, the minimal CD corresponds to  $\text{mod}(i + k/2, N) = 37.5$  for any  $k$ , indicating the time point within each step when the scanner is most unstable. This is an important finding because it is contrary to the expected situation where we would expect the most unstable region is close to the beginning of the step edge. The unstable region being shifted to the second half of the step is most likely caused by the communication between the scanner, the computer, and the detection device for synchronized data acquisition. According to this finding, the system should only utilize the first half of the step to provide improved imaging of multirange velocities. Therefore, we designed the camera trigger to capture only the A-scans when  $\text{mod}(i, N) < 25$  is satisfied. In this case, when skipping  $k$  A-scans within this set of A-scans, they would always meet the condition defined by  $\text{mod}(i + k/2, N) < 25$  [see bottom of Fig. 1(b), left region of vertical line]. Note that the scanner behavior is system dependent; thus, it is recommended that each system has to be individually optimized in order to use the step-scan to obtain variable velocity ranges.

Using the above optimized S-scan, we imaged a mouse brain *in vivo* with skull left intact. Figure 2(a) shows a typical B-scan DOCT image with  $k = 1$  using the mature Kasai algorithm.<sup>11</sup> To enhance the sensitivity, a high-pass filter was used prior to Doppler algorithm, assuming a linear superposition of stationary and moving scatters.<sup>12</sup> We employed a differential filter reported in ultrahigh sensitive OMAG,<sup>13</sup> which subtracts the complex OCT signals between adjacent A-scans to eliminate the static scattering signals

$$F(i) = S(i + 1) - S(i), \quad (1)$$

where  $i$  is the index of the A-scan number and  $S(i)$  is the complex signal of the  $i$ 'th A-scan. The Kasai method was then used to obtain the phase difference  $\phi$  by skipping  $k$  A-scans:  $\phi(k) = \angle\{\sum_i [F(i + k)F^*(i)]\}$ , where  $*$  denotes the complex conjugate. The result is shown in Fig. 2(b) where the nonflow area contains significant phase noise, resulted from the subtraction operation of Eq. (1). To extract meaningful Doppler signal, phase variance<sup>14,15</sup> is used to eliminate the noisy background, including phase-wrapped signals. Specifically, we calculated the phase variance

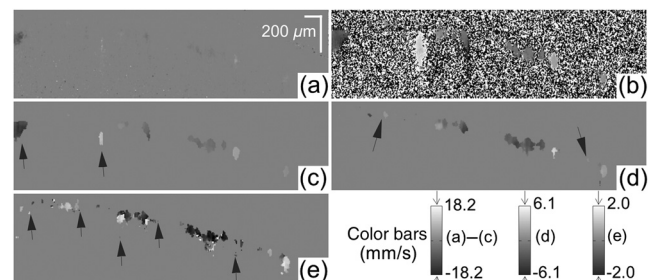


**Fig. 2** B-scan velocity images showing the process of mDOMAG of a mouse brain *in vivo*. (a) Conventional DOCT ( $k = 1$ ). (b) Differential filtered at  $k = 1$ . (c) After Kasai filtering of (b) and then masked at  $k = 1$ . (d) and (e) are the same as (c), but at  $k = 3$  and  $9$ , respectively.

of the filtered signal:  $P(k) = \sigma_r^2 \{ \angle [F(i+k)F^*(i)] \}$  to define a binary mask with a constant threshold  $R(k)$ . The values of  $R(k)$  are determined by the phase stability of the system, the flow variation status in the tissue, and the number of A-scans. With the current system setup, we determined  $R(k) = 2.4, 1.4, \text{ and } 0.4$  for  $k = 1, 3, \text{ and } 9$ , respectively. Thus, the final mDOMAG velocity image is given by

$$V(k) = \varphi(k) \cap [P(k) < R(k)]. \quad (2)$$

This operation has an additional advantage of eliminating fast flows that are beyond the capability of the system at a specific range of interest, causing phase wrapping in the phase signals. The final results are shown in Figs. 2(c)–2(e) for  $k = 1, 3, \text{ and } 9$ , respectively, where the Doppler signals for three velocity ranges were successfully extracted. The vessels with the fast flow are imaged in the  $k = 1$  range [arrows in Fig. 2(c)], while these vessels are disappeared in the  $k = 3$  range [Fig. 2(d)] due to their phase wrapping. The vessels with intermediate velocity (around 6 mm/s) start to emerge in the  $k = 3$  range [arrows in Fig. 2(d)]. In the slowest range of  $k = 9$ , numerous capillaries signals were seen [arrows in Fig. 2(e)], which are, however, beyond the detection capability of other ranges.

### 3 Results

Finally, we demonstrate the utility of the mDOMAG in the imaging of 3-D CBF within a mouse brain *in vivo*. In this experiment, we imaged  $2 \times 2$  tiles of  $2 \times 2 \text{ mm}^2$  areas of the mouse brain to obtain CBF mapping within an area of  $3.6 \times 3.6 \text{ mm}^2$ . The mosaic bidirectional en face maximum projection images for  $k = 1, 3, \text{ and } 9$  are given in Figs. 3(a), 3(b), and 3(c), showing the functional vessels in three velocity ranges of  $\pm 18.2, \pm 6.1, \text{ and } \pm 2.0 \text{ mm/s}$ , respectively. At  $k = 1$ , the velocity image mainly provides the vessels with the fast flows in the branches of MCA [pointed by arrows in Fig. 3(a)]. These branched arterioles are mostly disappeared in the velocity range of  $k = 3$  [Fig. 3(b)] due to their phase wrapping effect causing large phase variance, which is subsequently masked

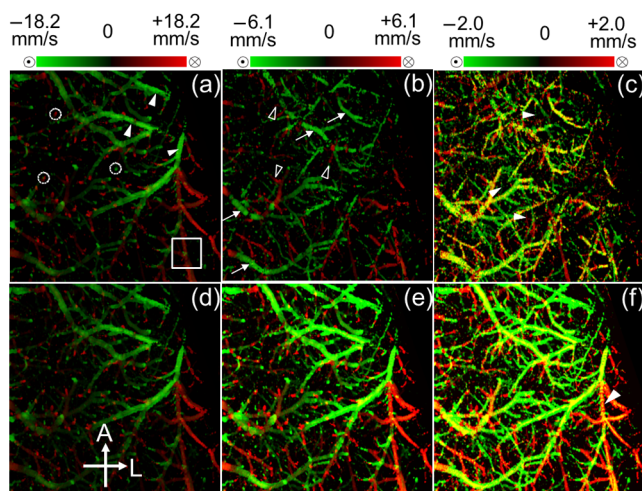


**Fig. 3** Bidirectional projection mDOMAG of a mouse brain *in vivo*. (a)–(c) The separately processed images at  $k = 1, 3, \text{ and } 9$ , respectively. (d)–(f) The combined velocity map but displayed with the same color bars as in (a)–(c), respectively. The imaging area is located between bregma and lambda at the right brain. A, anterior; L, lateral. White box =  $0.5 \times 0.5 \text{ mm}^2$ .

out by Eq. (2). The diving arterioles and rising venules appear as red and green isolated spots in Fig. 3(a) (e.g., marked by circles). This is because their flow directions are mainly parallel to the beam axis, giving their axial velocity large enough to be detected at this range. However, the surface vessels connected to them flow nearly perpendicularly to the probe beam, escaped the detection at  $k = 1$  but fell within the range for  $k = 3$  (e.g., hollow arrow heads). The venules that run almost parallel to the branched arterioles of the MCA over the surface of cortex are detected in Fig. 3(b) (pointed by the arrows), which have a velocity slower than the arterioles. At the smallest range [Fig. 3(c)], phase variance threshold is sufficient to keep all the slow flow signals, including capillaries (e.g., pointed by arrow heads). However, some out-of-range flow could not be completely removed, which is observed as phase-wrapped signals, seen as yellow color (combination of red and green). From the images with three different velocity ranges, we would be able to restore the complete vasculature. To restore, we combined the three 3-D mDOMAG maps into a single map with wide velocity range using a simple criterion:  $\text{mDOMAG} = V(k_C)$ , where  $k_C$  is the argument of the maximum of  $|V(k)|$ .

Figures 3(d)–3(f) show the combined data displayed with the same velocity ranges as in Figs. 3(a)–3(c), respectively. The vessel continuity is much improved when compared with the uncombined data. The slowest velocity range gives the best connectivity of the vessels, but the phase noise from the larger range data is amplified, resulting in some vessels appearing yellowish [arrow head in Fig. 3(f)]. This suggests that the monitoring of CBF within the cortex requires the investigation of both original and combined data. Overall, mDOMAG presents results with low noise, giving the maximal projection images with bidirectional multirange flow velocities and with high quality.

Note that flow velocity obtained after high-pass filtering deviates from the expected parabolic profile (Figs. 2 and 3). This phenomenon results from the overestimation of small Doppler signals affected by the differential filter.<sup>12</sup> Decreasing the cut-off frequency of the filter could lower overestimation, but at an expense of detecting more low-frequency components, which might instead cause underestimation. Also the assumption of linear contributions from different frequency components might not be optimal, leading to a biased Doppler estimation under high-pass filtering. Our future work will focus on compensating these errors or designing a new high-pass filter with less influence on the Doppler estimation. Also note that in the current study, we did not consider the relation between the degree of correlation and the fidelity of the Doppler signal<sup>16</sup> when imaging the CBF. Such relation can be important for *in vivo* applications, which might be useful to guide the optimization of scanning patterns to solve the limitations of the current approach.

### 4 Conclusion

In conclusion, we have demonstrated an optimized multirange DOMAG in which an S-scan protocol was used to achieve  $\sim 100\%$  correlation between repeated A-scans. High sensitivity and high quality bidirectional mDOMAG images with a wide velocity range were shown in mouse brain *in vivo* with skull left intact. It is recommended that to perform multiple velocity imaging using skipping, A-scan approach requires the characterization of the scanner in each individual system.

## Acknowledgments

The work was supported in part by the National Institutes of Health Grants (R01HL093140, and R01EB009682).

## References

1. R. K. Wang and L. An, "Doppler optical micro-angiography for volumetric imaging of vascular perfusion in vivo," *Opt. Express* **17**(11), 8926–8940 (2009).
2. H. C. Hendargo et al., "Doppler velocity detection limitations in spectrometer-based versus swept-source optical coherence tomography," *Biomed. Opt. Express* **2**(8), 2175–2188 (2011).
3. R. K. Wang et al., "Three dimensional optical angiography," *Opt. Express* **15**(7), 4083–4097 (2007).
4. Y. Jia and R. K. Wang, "Label-free in vivo optical imaging of functional microcirculations within meninges and cortex in mice," *J. Neurosci. Methods* **194**(1), 108–115 (2010).
5. Y. Jia and R. K. Wang, "Optical micro-angiography images structural and functional cerebral blood perfusion in mice with cranium left intact," *J. Biophoton.* **4**(1–2), 57–63 (2011).
6. H. Ren et al., "Cocaine-induced cortical microischemia in the rodent brain: clinical implications," *Mol. Psychiatry* **17**(10), 1017–1025 (2012).
7. F. Jaillon, S. Makita, and Y. Yasuno, "Variable velocity range imaging of the choroid with dual-beam optical coherence angiography," *Opt. Express* **20**(1), 385–396 (2012).
8. I. Grulkowski et al., "Scanning protocols dedicated to smart velocity ranging in spectral OCT," *Opt. Express* **17**(26), 23736–23754 (2009).
9. R. K. Wang and Z. Ma, "Real-time flow imaging by removing texture pattern artifacts in spectral-domain optical Doppler tomography," *Opt. Lett.* **31**(20), 3001–3003 (2006).
10. P. Meemon and J. P. Rolland, "Swept-source based, single-shot, multi-detectable velocity range Doppler optical coherence tomography," *Biomed. Opt. Express* **1**(3), 955–966 (2010).
11. D. Morofke et al., "Wide dynamic range detection of bidirectional flow in Doppler optical coherence tomography using a two-dimensional Kasai estimator," *Opt. Lett.* **32**(3), 253–255 (2007).
12. V. J. Srinivasan et al., "Quantitative cerebral blood flow with optical coherence tomography," *Opt. Express* **18**(3), 2477–2494 (2010).
13. L. An, J. Qin, and R. K. Wang, "Ultrahigh sensitive optical microangiography for in vivo imaging of microcirculations within human skin tissue beds," *Opt. Express* **18**(8), 8220–8228 (2010).
14. J. Fingler et al., "Mobility and transverse flow visualization using phase variance contrast with spectral domain optical coherence tomography," *Opt. Express* **15**(20), 12636–12653 (2007).
15. B. J. Vakoc et al., "Three-dimensional microscopy of the tumor micro-environment in vivo using optical frequency domain imaging," *Nat. Med.* **15**(10), 1219–1223 (2009).
16. J. Lee et al., "Dynamic light scattering optical coherence tomography," *Opt. Express* **20**(20), 22262–22277 (2012).